

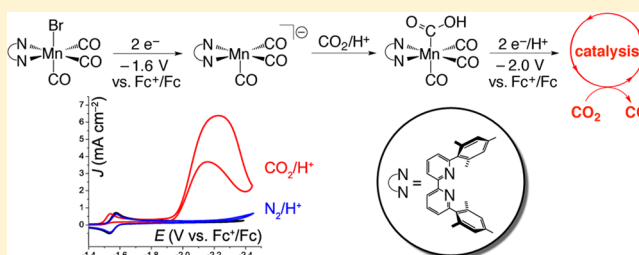
Manganese Catalysts with Bulky Bipyridine Ligands for the Electrocatalytic Reduction of Carbon Dioxide: Eliminating Dimerization and Altering Catalysis

Matthew D. Sampson, An D. Nguyen, Kyle A. Grice,[†] Curtis E. Moore, Arnold L. Rheingold, and Clifford P. Kubiak*

Department of Chemistry and Biochemistry, University of California, San Diego, 9500 Gilman Drive, Mail Code 0358, La Jolla, California 92093-0358, United States

S Supporting Information

ABSTRACT: With the goal of improving previously reported Mn bipyridine electrocatalysts in terms of increased activity and reduced overpotential, a bulky bipyridine ligand, 6,6'-dimesityl-2,2'-bipyridine (mesbpy), was utilized to eliminate dimerization in the catalytic cycle. Synthesis, electrocatalytic properties, X-ray diffraction (XRD) studies, and infrared spectroelectrochemistry (IR-SEC) of Mn(mesbpy)(CO)₃Br and [Mn(mesbpy)(CO)₃(MeCN)](OTf) are reported. Unlike previously reported Mn bipyridine catalysts, these Mn complexes exhibit a single, two-electron reduction wave under nitrogen, with no evidence of dimerization. The anionic complex, [Mn(mesbpy)(CO)₃][−], is formed at 300 mV more positive potential than the corresponding state is formed in typical Mn bipyridine catalysts. IR-SEC experiments and chemical reductions with KC₈ provide insights into the species leading up to the anionic state, specifically that both the singly reduced and doubly reduced Mn complexes form at the same potential. When formed, the anionic complex binds CO₂ with H⁺, but catalytic activity does not occur until a ~400 mV more negative potential is present. The Mn complexes show high activity and Faradaic efficiency for CO₂ reduction to CO with the addition of weak Brønsted acids. IR-SEC experiments under CO₂/H⁺ indicate that reduction of a Mn(I)–CO₂H catalytic intermediate may be the cause of this unusual “over-reduction” required to initiate catalysis.



INTRODUCTION

The catalytic reduction of carbon dioxide (CO₂) is a profoundly challenging problem that is of interest not only as a means of counteracting unsustainable emissions of CO₂ but also as a method for the development of renewable fuels and commodity chemicals.¹ Production of renewable liquid fuels through CO₂ reduction would circumvent declining supplies of fossil fuels and provide a fuel source capable of incorporation into existing infrastructure. Artificial photosynthetic systems are currently being developed that couple CO₂ reduction and water oxidation and are driven by solar energy.² When solar energy is harnessed, these systems will provide a route to carbon neutral energy. In order for large-scale photosynthetic devices to be practical, catalysts that favor proton-coupled CO₂ reduction over proton (H⁺) reduction must be optimized.³ Although direct production of liquid fuels is ideal,^{2,3} there are numerous homogeneous catalysts that efficiently reduce CO₂ to carbon monoxide (CO).^{1,4} This reduction pathway is useful for generating syngas (CO + H₂), which can be utilized in existing Fischer–Tropsch technologies to produce a wide variety of fuels and fuel precursors.⁵ CO is also a valuable reagent in methanol synthesis⁶ and in hydroformylation.⁷

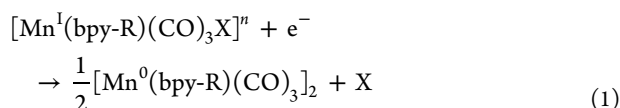
Of the systems that electrochemically reduce CO₂ to CO, *fac*-Re(bpy-R)(CO)₃X complexes (bpy-R = 4,4'-disubstituted-2,2'-bipyridine; X = halogen or solvent molecule with counteranion) are superior to most others in terms of rates, selectivities, and lifetimes.^{4c,d,f,g,i} Many studies have been performed to gain a detailed mechanistic understanding of these Re catalysts,⁸ including electrochemical studies,^{4c,g,i,9} X-ray crystallographic studies,^{4f,10} stopped-flow spectroscopy studies,^{4f,11} X-ray absorption spectroscopy (XAS) studies,¹² and theory.^{12,13} Since Re is one of the least abundant metals in the Earth's crust,¹⁴ we recently extended our CO₂ reduction studies to complexes based on Re's abundant first row counterpart, Mn.¹⁵ When considering a system for eventual scale-up and industrial use, Mn is much more appealing than Re because of cost and environmental ramifications.

The *fac*-Mn(bpy-R)(CO)₃X complexes, first reported by Bourrez et al. in 2011 to be active catalysts,¹⁶ have been shown to be viable alternatives to the aforementioned Re system as long as they are in the presence of weak Brønsted acids (namely, H₂O, methanol (MeOH), and 2,2,2-trifluoroethanol

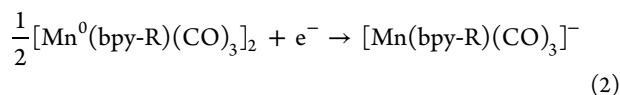
Received: February 5, 2014

Published: March 18, 2014

(TFE)). (Since all of the Mn and Re complexes discussed in this study are *fac*, this label will henceforth be omitted.) Specifically, Mn(bpy-R)(CO)₃X complexes are comparable in activity at similar conditions but offer the advantage of considerably lower overpotentials than the corresponding Re catalysts.^{15,16} Mn(bpy-^tBu)(CO)₃X maintains high activity in the presence of high concentrations of Brønsted acid (greater than 6000 equiv) while showing 100% Faradaic efficiency for the formation of CO. One distinct difference between these Mn catalysts and their Re counterparts is the tendency for dimerization after the first reduction.^{15,16} In the electrochemistry of Mn(bpy-R)(CO)₃X, two irreversible, one-electron reductions are observed, separated by 200–300 mV. A large oxidation peak occurs at more positive potentials after scanning through the first reduction. This indicates that a Mn–Mn dimer forms after rapid, irreversible loss of X. The two sequential one-electron reductions of typical Mn(bpy-R)(CO)₃X complexes are summarized in eqs 1 and 2:



where X = Br[−], n = 0 or X = MeCN, n = +1;



In contrast, for Re(bpy-R)(CO)₃X, the first one-electron reduction is reversible and loss of X is usually not observed until the second reduction. This tendency for dimerization is thought to contribute to an overpotential for two-electron reduction, as well as to limiting the activity of these Mn catalysts.¹⁵

In the studies described here, we sought to eliminate this dimerization pathway (eq 1) for the Mn(bpy-R)(CO)₃X catalysts and study the effects this has on catalytic overpotential and activity. We use a bulky bipyridine ligand, 6,6'-dimesityl-2,2'-bipyridine (mesbpy), to synthesize Mn(mesbpy)(CO)₃X. The mesbpy ligand was previously synthesized by Schmittel et al. and studied in regard to its Cu(I) coordination.¹⁷ We have previously utilized a similar bulky ligand, 6,6'-(2,4,6-triisopropylphenyl)-2,2'-bipyridine (tripbpy), to enforce tetrahedral geometries in late first row transition metal chlorides,¹⁸ as well as to isolate intermediates leading up to the catalytically active state in Re(bpy-R)(CO)₃X complexes.¹⁹ We report the synthesis, electrochemistry, infrared spectroelectrochemistry (IR-SEC), and X-ray crystallography of Mn(mesbpy)(CO)₃Br (**1**) and [Mn(mesbpy)(CO)₃(MeCN)](OTf) (**2**, MeCN = acetonitrile, OTf = trifluoromethanesulfonate). In the cyclic voltammograms (CVs), these complexes exhibit a single, reversible, two-electron reduction wave, with no evidence for dimerization. This behavior is distinctly different from the electrochemistry of typical Mn(bpy-R)(CO)₃X complexes, where two irreversible one-electron reductions are observed. For **1** and **2**, the usual second reduction has been shifted positive by ~300 mV and incorporated into a two-electron couple near the potential of the typical first reduction. A notable finding in this work is that complexes **1** and **2** show high activity for CO₂ reduction to CO but at ~400 mV more negative than the two-electron redox couple that generates the anionic, CO₂-binding state, [Mn(mesbpy)(CO)₃][−] (**4**). IR-SEC experiments under CO₂ and H⁺ indicate that reduction of

a Mn(I)–CO₂H catalytic intermediate may be the source of this “over-reduction” process required to initiate catalysis. By “over-reduction,” we mean that while **1** or **2** can be reduced by two electrons to form **4** and that while **4** shows clear evidence for binding and reducing CO₂/H⁺, catalysis is not initiated until a third electron is introduced at approximately −2.0 V vs Fc⁺/Fc. The studies and findings reported here provide new mechanistic and synthetic insights for improving catalysts in the future, with the ultimate goal of attaining a catalytic system capable of implementation on a large scale.

RESULTS AND DISCUSSION

Synthesis and Characterization. Synthesis of 6,6'-dimesityl-2,2'-bipyridine (mesbpy) was performed by the Suzuki coupling of 6,6'-dibromo-2,2'-bipyridine with mesitylboronic acid, as previously reported.¹⁷ Syntheses of Mn(mesbpy)(CO)₃Br (**1**) and [Mn(mesbpy)(CO)₃(MeCN)](OTf) (**2**) were performed analogous to previously reported procedures for Mn(bpy-R)(CO)₃X species.^{15,16,20} Complexes **1** and **2** were characterized by NMR, FTIR, and elemental analysis. Complex **1** was also characterized by X-ray crystallography. Singly reduced [Mn(mesbpy)(CO)₃]⁰ (**3**) and doubly reduced [Mn(mesbpy)(CO)₃][K(18-crown-6)] (**4**) were prepared by reduction of **1** in tetrahydrofuran (THF) by potassium-intercalated graphite (KC₈) (1.3 and 2.3 equiv, respectively), and anion **4** was characterized by NMR, FTIR, and X-ray crystallography. Paramagnetic **3** was characterized by IR spectroscopy; however, further characterization was not possible because of air sensitivity and short lifetime in solution.

Electrochemistry under N₂. Electrochemical experiments were performed to determine how the bulky bipyridine ligand affects the electrocatalytic properties of Mn(bpy-R)(CO)₃X complexes. The cyclic voltammograms of **1** (Figures S1 and S2 in Supporting Information) and **2** (Figure 1) in dry MeCN with 0.1 M tetrabutylammonium hexafluorophosphate (TBAPF₆) as the supporting electrolyte under an atmosphere of nitrogen (N₂) are distinctively different from previously reported electrochemistry of Mn(bpy)(CO)₃X, Mn(dmbpy)(CO)₃X (dmbpy = 4,4'-dimethyl-2,2'-bipyridine) and Mn-

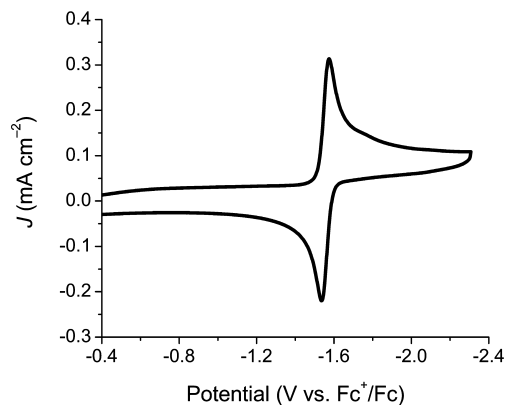


Figure 1. Cyclic voltammogram of 0.7 mM [Mn(mesbpy)(CO)₃(MeCN)](OTf) (**2**) in MeCN with 0.1 M TBAPF₆ as the supporting electrolyte under an atmosphere of N₂, showing one reversible, two-electron reduction of the complex. Scan rate is 100 mV/s. Working electrode is glassy carbon (3 mm diameter), counter electrode is a platinum wire, and pseudo-reference is a Ag/AgCl wire with ferrocene (Fc) added as an internal reference.

(bpy-^tBu)(CO)₃X.^{15,16} The CV of **2** consists of one reversible reduction wave at -1.55 V vs Fc⁺/Fc. Peak-to-peak separation of this reversible couple is 39 mV, compared to a peak-to-peak separation of 68 mV for Fc⁺/Fc in the same CV. This redox couple is best described as either an EEC or ECE mechanism, where two one-electron reductions occur combined with loss of a MeCN ligand. The second of the two one-electron reductions occurs either at the same or at a lower potential than the first reduction.²¹ This overall two-electron reduction leads to the anionic state, [Mn(mesbpy)(CO)₃]⁻ (**4**), as evidenced by chemical reductions and IR-SEC experiments (vide infra). For **2** in MeCN, digital simulations best support an EEC mechanism (Figure S7), where two one-electron reductions occur followed by loss of a MeCN ligand. Additionally, CVs of **2** feature an additional reduction at -2.25 V vs Fc⁺/Fc (Figure S9), likely corresponding to a bpy ligand-based reduction.

The corresponding two-electron reduction in CVs of **1** (peak-to-peak separation of 79 mV) is slightly less reversible than in CVs of **2** because of loss of Br⁻ to form the anionic state (Figures S1 and S2). The difference in peak-to-peak separation between **1** and **2** is likely due to the Br⁻ ligand causing a larger change of the total charge of the complex upon dissociation, as well as the difference in binding affinity of MeCN versus Br⁻. The scan rate dependence of the peak-to-peak separation in CVs of **1** and **2** is shown in Figure S6. IR-SEC experiments best support an ECE mechanism for complex **1** (vide infra), where loss of Br⁻ occurs directly after the first one-electron reduction.

Typically, CVs of Mn(bpy-R)(CO)₃X complexes exhibit two irreversible, one-electron reduction waves separated by 200–300 mV (depending on bpy substitution).^{15,16} The first reduction of Mn(bpy)(CO)₃Br (-1.6 V vs Fc⁺/Fc)¹⁶ is near the same potential as that of the reversible, two-electron couples of complexes **1** and **2** (-1.55 V vs Fc⁺/Fc). Incorporation of the bulky mesbpy ligand shifts the typical one-electron second reduction positive by ~ 300 mV so that this reduction is now merged with the first reduction as an overall two-electron couple. This represents a 300 mV decrease in the potential required to form the anionic state. For comparison, CVs of complex **1** and of Mn(bpy)(CO)₃Br, under identical conditions, are overlaid in Figure 2.

The electrochemistry of Mn(bpy-R)(CO)₃X complexes typically show a large oxidation wave at approximately -0.63 V vs Fc⁺/Fc after scanning through the first one-electron reduction (Figure 2).^{15,16} Lack of this oxidation peak and complete reversibility of the two-electron couple in the CVs of **1** and **2** suggests that dimerization has been completely eliminated by the bulky mesbpy ligand. Experiments with slower scan rates also show no evidence for dimerization (Figures S2 and S3). Complexes **1** and **2** are freely diffusing in solution according to Randles–Sevcik analysis (Figures S4 and S5).²²

Infrared Spectroelectrochemistry (IR-SEC) under N₂. IR-SEC of complex **1** under N₂ was performed to observe changes in accumulating species as the potential is scanned cathodically (Figure 3). At its resting state, **1** has three characteristic ν_{CO} stretches for facially coordinated tricarbonyl complexes at 2023, 1936, and 1913 cm⁻¹. When voltage is applied at the potential of the two-electron reduction seen in CVs (approximately -1.6 V vs Fc⁺/Fc), we see growth of ν_{CO} stretches at 1973, 1883, 1866, and 1808 cm⁻¹, decay of ν_{CO} stretches at 2023 and 1936 cm⁻¹, and a shift of the ν_{CO} stretch at 1913 cm⁻¹ to slightly lower energy.

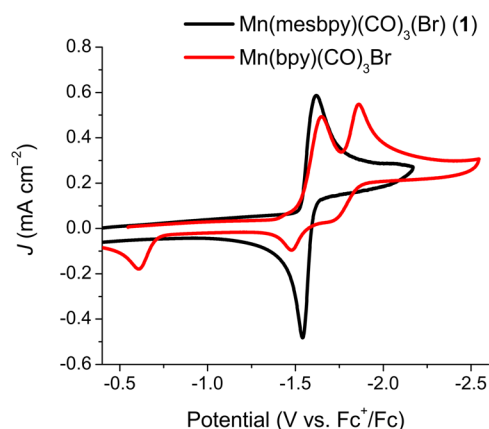


Figure 2. Comparison of the cyclic voltammograms of Mn(mesbpy)(CO)₃Br (**1**) and Mn(bpy)(CO)₃Br under identical conditions (1 mM complex). Each experiment is performed in MeCN with 0.1 M TBAPF₆ as the supporting electrolyte, under an atmosphere of N₂, at a scan rate of 100 mV/s, with a glassy carbon working electrode (3 mm diameter), with a platinum wire counter electrode, with a Ag/AgCl wire pseudo-reference, and with Fc added as an internal reference.

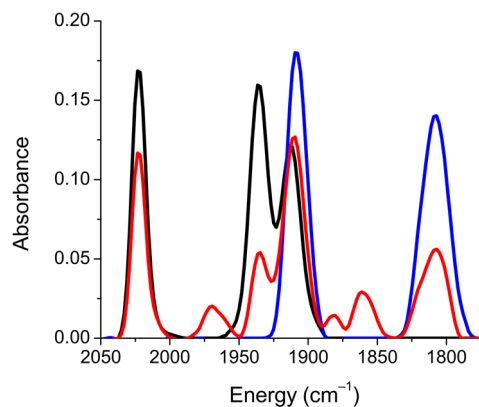


Figure 3. IR-SEC of 3 mM **1** in MeCN with 0.1 M TBAPF₆ electrolyte under an atmosphere of N₂. The resting species (black, **1**) has three ν_{CO} stretches at 2023, 1936, and 1913 cm⁻¹. Upon initial reduction at approximately -1.6 V (red), singly reduced species **3** (1973, 1883, 1866 cm⁻¹) and doubly reduced species **4** (1909 and 1808 cm⁻¹) form. When the voltage of the cell is held at approximately -1.6 V for more than 1 min, all species are converted to **4** (blue).

The ν_{CO} stretches at 1973, 1883, and 1866 cm⁻¹ are indicative of a singly reduced Mn complex, assigned as [Mn(mesbpy)(CO)₃]⁰ (**3**). A shift of the high-energy ν_{CO} stretch from 2023 to 1973 cm⁻¹ (~ 50 cm⁻¹ shift to lower energy) is observed between **1** and this singly reduced complex. This shift is very similar to the shift observed in five-coordinate [Re(bpy-R)(CO)₃]⁰ complexes, with no bound X,⁴⁸ and agrees well with our chemical reductions with KC₈ (vide infra). The ν_{CO} stretches at 1909 and 1808 cm⁻¹ in the IR-SEC are indicative of a doubly reduced [Mn(mesbpy)(CO)₃]⁻ species (**4**), which binds CO₂ in electrocatalysis studies (vide infra). A shift of the high-energy ν_{CO} stretch from 2021 to 1917 cm⁻¹ (~ 100 cm⁻¹ shift to lower energy) is observed between **1** and **4**. The ν_{CO} stretches of this species match well with those for the anionic [Mn(mesbpy)(CO)₃]⁻ complex produced by the chemical reduction of **1** with KC₈ (1917 and 1815 cm⁻¹, vide infra) and also match well with previously reported anionic [Mn(bpy-R)(CO)₃]⁻ complexes.^{15,23}

Both species **3** and **4** grow in at the same potential, and there is very small accumulation of the ν_{CO} stretches corresponding to singly reduced **3**. When voltage is held at approximately -1.6 V vs Fc^+/Fc for more than 1 min, all singly reduced species is converted to doubly reduced species, **4**. Because a singly reduced species is observed in these IR-SEC experiments, we believe that the reversible couple seen in CVs is the result of two one-electron reductions that occur at the same potential instead of a direct two-electron reduction. Chemical reduction experiments (vide infra) and computer simulations (Figure S7) also support two one-electron reductions. These observations in IR-SEC are consistent with an ECE mechanism for **1**, where a single-electron reduction and loss of Br^- occurs followed by a second one-electron reduction resulting in the formation of complex **4**.

Chemical Reductions. In addition to IR-SEC studies providing insights into the species leading up to the catalytically active state, complexes **3** and **4** can be prepared via chemical reduction with KC_8 . Reduction of **1** with ~ 1 equiv of KC_8 in THF produces singly reduced **3**. For this one-electron reduction from **1** to **3**, the high-energy ν_{CO} stretch shifts by ~ 44 cm^{-1} to lower energy (2021 to 1984 cm^{-1}). This shift is very similar to the shift observed in the IR-SEC of $\text{Re}(\text{bpy-R})(\text{CO})_3\text{X}$ complexes, where the high energy ν_{CO} stretch shifts ~ 40 cm^{-1} lower in energy to form the neutral five-coordinate $\text{Re}(0)\text{bpy}(0)$ species with no bound X.^{4f} Likewise, the average of the two low-energy ν_{CO} stretches shifts by ~ 36 cm^{-1} to lower energy. Because of the similar IR features between this complex and our singly reduced Mn complex, we are assigning our singly reduced species as $[\text{Mn}(\text{mesbpy})(\text{CO})_3]^0$ (**3**) with no bound Br^- or solvent molecule. This one-electron reduction is in agreement with one-electron reductions of other Mn complexes, where loss of halide occurs rapidly,¹⁵ except that the mesbpy ligand inhibits dimerization at the sixth coordination position. DFT-calculated ν_{CO} stretches of **3** agree very well with the experimental ν_{CO} stretches (see Supporting Information). Complex **3** has a relatively short lifetime in THF solution. Although we were able to obtain an IR spectrum of **3**, this complex disproportionates into various species, including a Mn(I) complex and complex **4**, over the course of hours. Unreduced **1** and doubly reduced **4** are much more stable than singly reduced **3**, giving rise to a net two-electron reduction in CVs of **1** and **2**.

Additionally, the two-electron reductions in CVs of **1** and **2** in THF solution show much larger peak-to-peak separations than the corresponding reductions in MeCN solution (Figure S8). Specifically, a peak-to-peak separation of ~ 300 mV is observed for this reduction in the CV of **2** in THF. This peak-to-peak separation further supports the assignment of complex **3** as five-coordinate $[\text{Mn}(\text{mesbpy})(\text{CO})_3]^0$. In MeCN, species **3** is likely very unstable, as evidenced by the peak-to-peak separations in CVs of **1** and **2** in MeCN (39 and 79 mV, respectively). However, in THF solution, this species is stable long enough to obtain spectroscopic analysis.

Reduction of **1** with >2 equiv of KC_8 in THF produces anion **4** and results in a shift of the high-energy ν_{CO} stretch from 2021 to 1917 cm^{-1} (~ 100 cm^{-1} shift to lower energy). Additionally, the average of the two low-energy ν_{CO} stretches of **3** shifts to the low-energy broad ν_{CO} stretch of **4**, a ~ 72 cm^{-1} shift to lower energy, from ~ 1887 to 1815 cm^{-1} . These ν_{CO} stretches match those observed in our IR-SEC studies (1909 and 1808 cm^{-1}) and are indicative of a doubly reduced $[\text{Mn}(\text{mesbpy})(\text{CO})_3]^-$ complex (**4**). The ν_{CO} stretches for **4** match well with

previously reported anionic $[\text{Mn}(\text{bpy-R})(\text{CO})_3]^-$ complexes;^{15,23} however, these ν_{CO} stretches are shifted to lower energy when compared to $[\text{Re}(\text{bpy-R})(\text{CO})_3]^-$ complexes.^{4f,10d} Bond length alternation in the bpy ring in the crystal structure of **4** (vide infra) and DFT calculations (see Supporting Information) indicate that significant electron density resides on the bpy ring, although the low-energy ν_{CO} stretches indicate that M–CO back bonding is notably increased in these Mn anions compared to the analogous Re anions. The FTIR spectra of **1**, **3**, and **4** are shown in Figure 4.

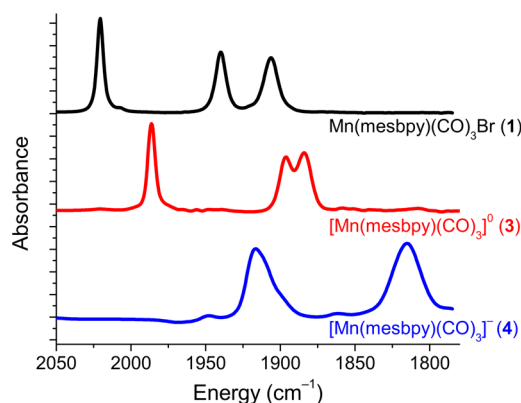


Figure 4. FTIR spectra of $\text{Mn}(\text{mesbpy})(\text{CO})_3\text{Br}$ (black, **1**), $[\text{Mn}(\text{mesbpy})(\text{CO})_3]^0$ (red, **3**), and $[\text{Mn}(\text{mesbpy})(\text{CO})_3]^-[\text{K}(18\text{-crown-6})]$ (blue, **4**) in THF, showing high correlation to species observed in IR-SEC studies.

X-ray Crystallography. We have had success growing crystals of the parent and anionic species of both $\text{Re}(\text{bpy-R})(\text{CO})_3\text{X}$ and $\text{Mn}(\text{bpy-R})(\text{CO})_3\text{X}$ complexes.^{4f,10d,15} X-ray quality crystals of complex **1** were grown by vapor diffusion of pentane into a THF solution of the complex (Figure 5). Complex **1** crystallized in the space group C_2/c with eight independent molecules in the unit cell. Attempts to crystallize singly reduced **3** were not successful, as this species is not long-lived in solution. Specifically, any attempts at growing crystals of **3** resulted in a mixture of crystals of a Mn(I) complex and complex **4**. DFT calculations on **3** show a five-coordinate, unsaturated monomer with a HOMO delocalized across the bpy ligand and the Mn center (Figure S30). Reduction of **1** by >2 equiv of KC_8 in the presence of 18-crown-6 results in loss of bromide, forming the anionic complex **4**. 18-Crown-6 was added during reduction to inhibit potassium coordination to the carbonyl ligands of **4**. The crystal structure of **4** was obtained from the vapor diffusion of pentane into a THF solution of the complex (Figure 6). Complex **4** is a five-coordinate, unsaturated anion with a $[\text{K}^+(18\text{-crown-6})]$ counteranion. In this structure, the $[\text{K}^+(18\text{-crown-6})(\text{THF})]$ fragment has positional disorder over two positions (Figure 6 and Figure S10); however, the Mn anion fragment, the pertinent fragment for this study, is modeled without disorder. The geometry of anion **4** is square pyramidal (slightly skewed from a perfect square pyramid) with $\tau_5 = 0$ ($\tau_5 = 0$ for a perfect square pyramid and $\tau_5 = 1$ for a perfect trigonal bipyramid).²⁴ X-ray diffraction structures of most other Re and Mn bipyridine anions are between square pyramidal and trigonal bipyramidal.^{4f,10d,15} Specifically, $[\text{Re}(\text{bpy-}^t\text{Bu})(\text{CO})_3][\text{K}(18\text{-crown-6})]$ and $[\text{Mn}(\text{bpy-}^t\text{Bu})(\text{CO})_3][\text{K}(18\text{-crown-6})]$ are five coordinate and have a $\tau_5 = 0.46$ and $\tau_5 = 0.53$, respectively.^{4f,15} The bulky mesbpy ligand on **4** seems to prevent the carbonyls from

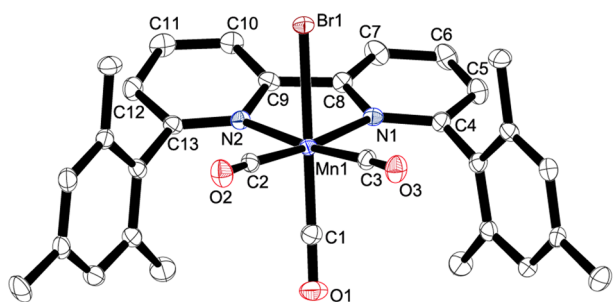


Figure 5. Molecular structure of $\text{Mn}(\text{mesbpy})(\text{CO})_3\text{Br}$ (**1**), with hydrogen atoms omitted for clarity. Ellipsoids are set at the 50% probability level. Platon's SQUEEZE was used to remove a disordered THF solvent molecule from the asymmetric unit in the crystal structure. Relevant distances (Å) and bond angles (deg) are the following: Mn1–Br1, 2.5298(6); Mn1–N1, 2.090(2); Mn1–N2, 2.084(2); Mn1–C1, 1.795(3); Mn1–C2, 1.809(3); Mn1–C3, 1.816(3); C1–O1, 1.147(3); C2–O2, 1.150(3); C3–O3, 1.142(3); N1–C4, 1.351(3); C4–C5, 1.393(4); C5–C6, 1.379(4); C6–C7, 1.380(4); C7–C8, 1.378(3); N1–C8, 1.366(3); C8–C9, 1.473(4); N2–C9, 1.364(3); C9–C10, 1.387(4); C10–C11, 1.375(4); C11–C12, 1.378(4); C12–C13, 1.387(4); N2–C13, 1.358(3); Br1–Mn1–N1, 84.90(6); Br1–Mn1–N2, 86.16(6); Br1–Mn1–C1, 176.71(9); Br1–Mn1–C2, 88.06(8); Br1–Mn1–C3, 87.54(8); N1–Mn1–N2, 79.35(8); N1–Mn1–C1, 97.63(10); N1–Mn1–C2, 172.96(10); N1–Mn1–C3, 99.25(10); N2–Mn1–C1, 96.35(10); N2–Mn1–C2, 100.28(10); N2–Mn1–C3, 173.64(10); C1–Mn1–C2, 89.39(12); C1–Mn1–C3, 89.98(12); C2–Mn1–C3, 80.34(11).

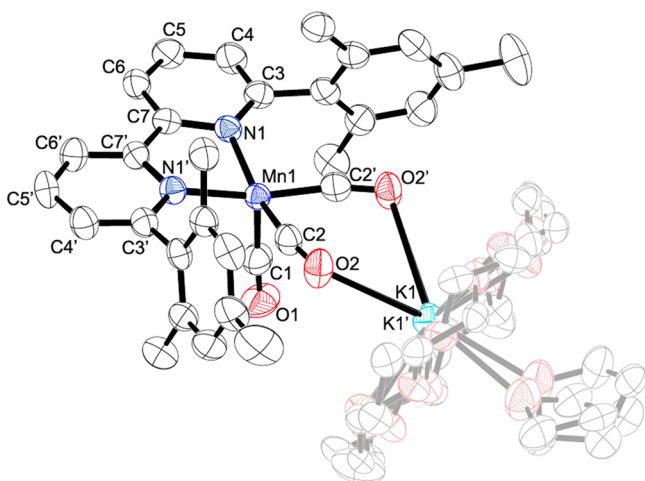


Figure 6. Molecular structure of $[\text{Mn}(\text{mesbpy})(\text{CO})_3][\text{K}(18\text{-crown-6})(\text{THF})]$ (**4**), with hydrogen atoms omitted for clarity. The counteranion, $[\text{K}^+(18\text{-crown-6})]$, and THF solvent molecules are shown as partially transparent in order to emphasize the $[\text{Mn}(\text{mesbpy})(\text{CO})_3]^-$ anion. The $[\text{K}^+(18\text{-crown-6})(\text{THF})]$ fragment has positional disorder over two positions (Figure S10). Ellipsoids are set at the 50% probability level. Relevant distances (Å) and bond angles (deg) are the following: Mn1–N1, 2.005(4); Mn1–C1, 1.770(9); Mn1–C2, 1.783(6); C1–O1, 1.162(10); C2–O2, 1.178(7); N1–C3, 1.386(7); N1–C7, 1.389(6); C3–C4, 1.355(8); C4–C5, 1.417(8); C5–C6, 1.367(8); C6–C7, 1.399(7); C7–C7', 1.424(10); N1–Mn1–N1', 79.7(2); C1–Mn1–N1, 104.6(2); C1–Mn1–C2, 91.4(3); N1–Mn1–C2, 99.7(2); N1–Mn1–C2', 163.7(2); C2–Mn1–C2', 76.2(3).

rearranging toward trigonal bipyramidal, resulting in an almost ideal square pyramid. The X-ray crystal structure of **4** is nearly identical to that of its DFT-calculated structure (Figure S31).

X-ray crystallography of **1** and **4** provides insight into the amount of electron density stored on the noninnocent bpy ligand. In the crystal structure of **4**, bond length alternation and the short inter-ring $\text{C}_{\text{py}}\text{--}\text{C}_{\text{py}}$ bond in the bpy ligand are indicative of significant electron density on this noninnocent ligand (Figure 6).²⁵ The inter-ring $\text{C}_{\text{py}}\text{--}\text{C}_{\text{py}}$ bond shortens from 1.473 Å in the crystal structure of **1** to 1.424 Å in **4**. This inter-ring $\text{C}_{\text{py}}\text{--}\text{C}_{\text{py}}$ bond of **4** agrees well with previously reported crystal structures of $[\text{Mn}(\text{bpy}^t\text{Bu})(\text{CO})_3]^-$ and $[\text{Mn}(\text{bpy})(\text{CO})_3]^-$ (1.413 and 1.418 Å, respectively).^{15,23} Our recent XAS and computational studies on similar $[\text{Re}(\text{bpy-R})(\text{CO})_3]^-$ complexes have determined that these anions possess formally $\text{Re}(0)\text{bpy}(1^-)$ ground states.¹² The crystal structure of **4** shows high similarity to that of many $[\text{Re}(\text{bpy-R})(\text{CO})_3]^-$ complexes. Recent DFT calculations by Scarborough et al.²⁶ and Hartl et al.²³ have characterized the $[\text{Mn}(\text{bpy})(\text{CO})_3]^-$ anion as a singlet diradical $\text{Mn}(\text{I})\text{bpy}(2^-)$ complex with significant π -donation of the electron density from a $\text{bpy}(2^-)$ dianion to a Mn(I) ion. Scarborough et al. explains that this π -donation results in a crystal structure with $\text{C}_{\text{py}}\text{--}\text{C}_{\text{py}}$ distances that resemble a $\text{bpy}(1^-)$ radical anion, which would imply a Mn(0) center. Both this computational and our experimental analyses are consistent with a significant amount of electron density on the bpy-R ligand. In contrast to the aforementioned calculations, the increased Mn–CO back bonding observed by IR spectroscopy could indicate that less electron density lies on the bpy ligand in **4** and other $[\text{Mn}(\text{bpy-R})(\text{CO})_3]^-$ anions compared to similar Re anions (which have $\text{Re}(0)\text{bpy}(1^-)$ formal ground states). The noninnocence of the bpy ligand helps explain the high selectivity of $\text{M}(\text{bpy-R})(\text{CO})_3\text{X}$ ($\text{M} = \text{Mn}$ or Re) catalysts for the reduction of CO_2 in the presence of significant concentrations of H^+ , where electron density on the bpy ligand favors transferring two electronic charges to CO_2 through both σ and π interactions.¹²

Electrocatalysis. The electrocatalytic properties of **1** and **2** were studied in a custom-made, single-compartment, airtight cell with a glassy carbon working electrode, Pt wire counter electrode, and a Ag/AgCl wire pseudo reference electrode separated from the main compartment by a Vycor tip. The electrochemical solution was sparged with CO_2 until gas saturation ($\sim 0.28 \text{ M}$).²⁷ CVs of complexes **1** and **2** did not change under CO_2 in dry MeCN (Figure 7, Figures S11–S13). However, addition of weak Brønsted acid (H_2O , MeOH, or TFE) to **2** resulted in an increase in current at approximately -2.0 V vs Fc^+/Fc , i.e., $\sim 400 \text{ mV}$ after the two-electron reduction that generates anionic species **4** (Figure 7, Figures S11–S14). This current increase corresponds to the electrocatalytic reduction of CO_2 to CO , as verified by controlled potential electrolysis (CPE) (vide infra). No current increase was observed in the CV of **2** under N_2 with added weak acid, indicating that the current increase is not due to proton reduction (Figure 7, Figure S13). Higher concentrations of weak Brønsted acid in CO_2 reduction electrocatalysis experiments resulted in increased current densities, before reaching a peak current density and leveling off or dropping with addition of more H^+ (Figure 8, Figure S12, and Figure S14 for MeOH, H_2O , and TFE, respectively). Addition of weak acid to **1** resulted in very similar trends in CVs (Figure S11).

For a reversible electron-transfer reaction followed by a fast catalytic reaction ($\text{E}_\text{R}\text{C}_\text{cat}$ scheme), the peak catalytic current (i_cat) is given by eq 3.²⁸

$$i_\text{cat} = n_\text{cat}FA[\text{cat}](Dk_\text{cat}[\text{Q}]^y)^{1/2} \quad (3)$$

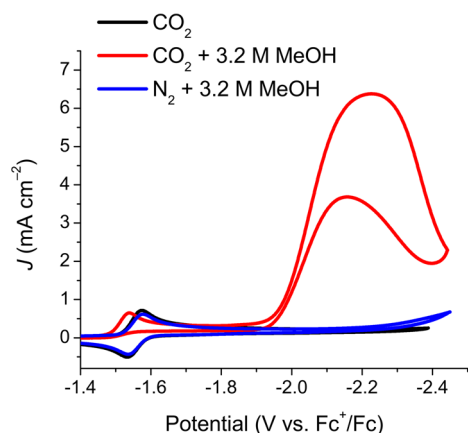


Figure 7. Cyclic voltammograms (CVs) showing catalytic current for 1 mM $[\text{Mn}(\text{mesbpy})(\text{CO})_3(\text{MeCN})](\text{OTf})$ (**2**) under CO_2 with added MeOH (red). This current increase is due solely to the electrocatalytic reduction of CO_2 to CO. Under N_2 with added MeOH, no current increase is observed (blue), which is similar to the CV under CO_2 with no added MeOH (black). CVs were taken in 0.1 M TBAPF₆/MeCN with a scan rate of 100 mV/s, a glassy carbon working electrode (3 mm diameter), a platinum wire counter electrode, and a Ag/AgCl wire pseudo-reference with ferrocene (Fc) added as an internal reference.

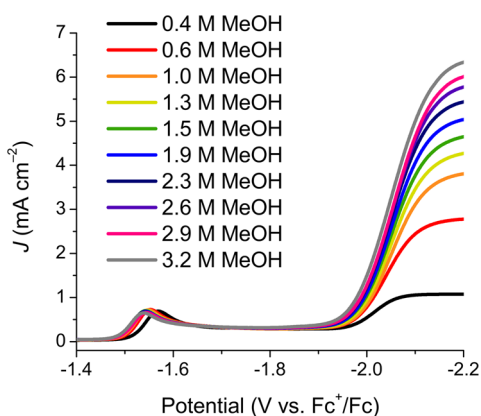


Figure 8. Linear scan voltammograms showing the electrocatalytic reduction of CO_2 to CO by 1 mM $[\text{Mn}(\text{mesbpy})(\text{CO})_3(\text{MeCN})](\text{OTf})$ (**2**) in 0.1 M TBAPF₆/MeCN with addition of MeOH. The solution is under an atmosphere of, and saturated with (~ 0.28 M), CO_2 . Voltammograms are taken at a scan rate of 100 mV/s.

The derivation of eq 3 assumes that pseudo-first-order kinetics apply; i.e., the reaction is first order in catalyst and that the concentrations of the substrates Q are large in comparison to the concentration of catalyst. In eq 3, n_{cat} is the number of electrons required for the catalytic reaction ($n_{\text{cat}} = 2$ for the reduction of CO_2 to CO), F is Faraday's constant, A is the surface area of the electrode, $[\text{cat}]$ is the catalyst concentration, D is the diffusion constant of the catalytically active species, k_{cat} is the rate constant of the catalytic reaction, and $[\text{Q}]$ is the substrate concentrations. Plotting i_{cat} versus the square root of $[\text{CO}_2]$ shows a linear relationship, indicating that the catalytic reaction is first order in $[\text{CO}_2]$ (Figure S21). Additionally, plots of i_{cat} versus $[\text{H}^+]$ show second-order dependence on $[\text{H}^+]$ at low $[\text{H}^+]$ (Figure S22). At high $[\text{H}^+]$, i_{cat} reaches a limiting value independent of $[\text{H}^+]$ (Figures S22–S24), which is typical of saturation kinetics expected for catalytic reactions.²⁹ Electrocatalytic reactions are also first order in $[\text{cat}]$, as evidenced by plotting i_{cat} vs $[\text{cat}]$ (Figures S25 and S26). The

initial catalytic current plateaus are relatively scan rate independent for all CVs with added H_2O , MeOH, and TFE (Figures S17, S18, and S20). In summary, at high $[\text{H}^+]$, the electrocatalytic reduction of CO_2 is first order in catalyst, first order in CO_2 , independent of acid concentration, and at steady state conditions.

Equation 4 describes the peak current of a complex with a reversible electron transfer and with no following reaction.³⁰

$$i_p = 0.4463n_p^{3/2}FA[\text{cat}]\left(\frac{F}{RT}\right)^{1/2}v^{1/2}D^{1/2} \quad (4)$$

In eq 4, R is the universal gas constant, T is temperature, n_p is the number of electrons in the reversible, noncatalytic reaction, and v is scan rate (0.1 V/s). Dividing eq 3 by eq 4 allows for the determination of i_{cat}/i_p and allows further calculation of the catalytic rate constant (k_{cat}) and the turnover frequency (TOF), as shown in eq 5.

$$\text{TOF} = k_{\text{cat}}[\text{Q}] = \frac{Fv n_p^3}{RT} \left(\frac{0.4463}{n_{\text{cat}}}\right)^2 \left(\frac{i_{\text{cat}}}{i_p}\right)^2 \quad (5)$$

In this equation, A cancels out because the same electrode was used for the experiments under CO_2 and N_2 . D also cancels out because we are assuming that the diffusion constant of the catalytically active species does not change significantly under CO_2 or N_2 .

Using eqs 3–5, we can calculate peak i_{cat}/i_p and TOF values for catalyst **2** with added H_2O , MeOH, or TFE. For these calculations, i_p is determined as the peak current under N_2 with an amount of weak Brønsted acid corresponding to peak i_{cat} conditions. Addition of H_2O ($\text{p}K_a = 31.4$ in DMSO)³¹ to a 1 mM solution of **2** under CO_2 resulted in a peak $i_{\text{cat}}/i_p = 20$ (4.8 mA/cm² peak current density) and TOF = 700 s⁻¹ at 3.5 M H_2O . Addition of MeOH or TFE ($\text{p}K_a$ of 29.0³¹ and 23.5,³² respectively, in DMSO) leads to higher peak current densities under CO_2 . (Note: Literature values for $\text{p}K_a$ values of H_2O , MeOH, and TFE in MeCN are not reported; however, these values can be estimated accordingly from $\text{p}K_a$ values in DMSO.) Specifically, addition of MeOH resulted in a peak $i_{\text{cat}}/i_p = 30$ (7.6 mA/cm² peak current density) and TOF = 2000 s⁻¹ at 3.2 M MeOH. Addition of TFE resulted in a peak $i_{\text{cat}}/i_p = 50$ (13 mA/cm² peak current density) and a TOF = 5000 s⁻¹ at 1.4 M TFE. Calculated i_{cat}/i_p and TOF values for **2** and previously reported Mn(bpy-^tBu)(CO)₃Br are listed in Table 1. Catalyst **2** is more active than the most active Mn bpy catalyst previously reported, Mn(bpy-^tBu)(CO)₃Br, under MeOH and TFE. However, **2** is slightly less active than Mn(bpy-^tBu)(CO)₃Br under H_2O . Particularly, under identical conditions with 1.4 M TFE, catalyst **2** is ~ 1.2 times more active than Mn(bpy-^tBu)(CO)₃Br.

A notable feature of the catalytic CVs of **1** and **2** is the pronounced deviation from a steady state “S-shaped” wave (Figure 7, Figure S13). The peak maximum at approximately -2.2 V vs Fc^+/Fc and especially the peak in the return oxidation (approximately -2.1 V vs Fc^+/Fc) are quite unusual and deserve comment. These unusual characteristics likely arise from multiple factors. The main factor contributing to this odd current response is an overlapping bpy-based reduction at approximately -2.3 V vs Fc^+/Fc (Figures S9, S15, S19). At a scan rate of 100 mV/s, this additional reduction feature cannot be distinguished from the catalytic current response (Figures 7, S13, S15, and S19). However, at higher scan rates, this

Table 1. Comparison of Peak $i_{\text{cat}}/i_{\text{p}}$ and TOF Values for Both $[\text{Mn}(\text{mesbpy})(\text{CO})_3(\text{MeCN})](\text{OTf})$ (2**) and $[\text{Mn}(\text{bpy-}^t\text{Bu})(\text{CO})_3\text{Br}]$ in MeCN (1 mM each catalyst)^a**

Brønsted acid	$[\text{Mn}(\text{mesbpy})(\text{CO})_3(\text{MeCN})](\text{OTf})$ (2)			$\text{Mn}(\text{bpy-}^t\text{Bu})(\text{CO})_3\text{Br}$		
	$[\text{acid}]^b$ (M)	$i_{\text{cat}}/i_{\text{p}}^c$	TOF (s^{-1})	$[\text{acid}]^d$ (M)	$i_{\text{cat}}/i_{\text{p}}^e$	TOF (s^{-1})
H ₂ O	3.5	20	700	3.1	25	1100
MeOH	3.2	30	2000	5.8	26	1100
TFE	1.4	50	5000	1.4	42	3000

^aSolutions are saturated with (approximately 0.19–0.28 M) and under an atmosphere of CO₂ with added weak Brønsted acids. Data are taken from voltammograms at a scan rate of 100 mV/s. [CO₂] is approximately 0.28 M in dry MeCN, 0.26 M in 3.5 M H₂O, 0.27 M in 3.2 M MeOH, and 0.27 M in 1.4 M TFE.²² ^b[Acid] at highest $i_{\text{cat}}/i_{\text{p}}$ for **2**. ^c $i_{\text{cat}}/i_{\text{p}}$ values are calculated at equal [acid]. ^d[Acid] at highest $i_{\text{cat}}/i_{\text{p}}$ for $\text{Mn}(\text{bpy-}^t\text{Bu})(\text{CO})_3\text{Br}$. ^eValues taken from ref 15.

reduction feature becomes apparent (Figures S15, S16, S19). The catalytic current plateaus, directly before the bpy-based reduction (Figures S15–S20), are fairly scan rate independent. The scan rate dependences of the catalytic current plateaus are shown in Figures S17, S18, and S20 (for added H₂O, MeOH, and TFE, respectively).

Additionally, diffusional characteristics (peaks) in catalytic CVs under slow scan rates can be ascribed to side phenomena.^{4b,33} These side phenomena are generally side reactions that are generated by the catalytic reaction but that compete with this catalytic reaction.³³ The fact that the catalytic wave occurs at a potential beyond the formally Mn(I/–I) prewave, where no electrochemical process is observed in the absence of CO₂/H⁺, indicates that this catalytic wave involves the reduction of a species that does not exist without CO₂/H⁺. In view of the formally Mn(I/–I) prewave dependence of CO₂ concentration (vide infra), this species is likely the hydroxycarbonyl complex $\text{Mn}(\text{mesbpy})(\text{CO})_3(\text{CO}_2\text{H})$ (vide infra). This 18-e[–] complex appears to be stable until it is reduced by a third e[–] in a likely bpy-based reduction. This reduction presumably labilizes the CO₂H[–] group to form CO and [–]OH, the latter of which rapidly reacts with H⁺ in solution. This has the effect of raising the pH in the reaction diffusion layer. The subsequent reduction of a Mn(I) complex and reaction with CO₂/H⁺ to form another Mn–CO₂H species further raises the local pH and depletes CO₂. In addition, since the source of the H⁺ is a weak acid, the conjugate base RO[–] should be capable of binding a second equivalent of CO₂ to give the alkyl carbonate ROCO_2^- , further depleting the CO₂ concentration. These side reactions compete with catalysis for the same substrates and have the effect of decreasing overall rates of catalysis. Lastly, if catalysis can occur only upon bpy-based reduction of $\text{Mn}(\text{mesbpy})(\text{CO})_3(\text{CO}_2\text{H})$, then this reduction process should show diffusional characteristics, as should the return oxidation of the radical anion. These side reactions along with the overlapping bpy-based reduction at approximately –2.3 V vs Fc⁺/Fc are likely the origins of the unusual catalytic wave shape. A more detailed relation between the catalytic mechanism and appearance of the catalytic wave in this system is beyond the scope of this article and will be the subject of ongoing investigation.

CPE was performed on **2** at –2.2 V vs Fc⁺/Fc to measure the efficiency at which CO is produced and to gain insights into the lifetime of the catalyst. Gas chromatography indicates that no hydrogen is formed during these experiments, and catalyst **2**

operates with a Faradaic efficiency of 98 ± 6% for the formation of CO from CO₂, measured for the first ~4 turnovers of the catalyst (first ~70 min of catalysis, based on total catalyst concentration in cell) (Figure 9). These CPE experiments were

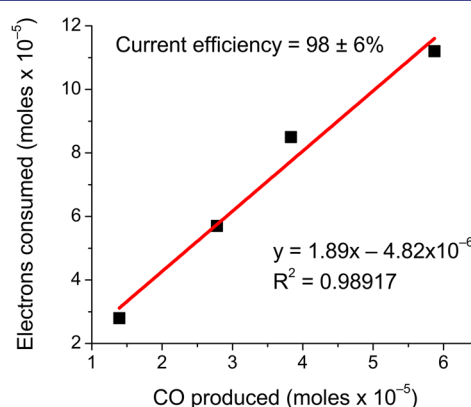


Figure 9. Production of CO from CO₂ by 0.5 mM $[\text{Mn}(\text{mesbpy})(\text{CO})_3(\text{MeCN})](\text{OTf})$ (**2**) during controlled potential electrolysis at –2.2 V vs Fc⁺/Fc with 0.3 M TFE. The slope of ~2 represents a Faradaic efficiency of 98 ± 6%. After a steady state current was reached, bulk electrolysis of this solution showed no significant current degradation over the course of several hours.

performed with 0.5 mM **2** and 0.3 M TFE with a carbon rod working electrode (surface area of 7.4 cm²). Although Faradaic efficiency was only recorded for the first 70 min of catalysis, the lifetime of catalyst **2** is much greater than this, as evidenced by the CPE trace in Figure S27. The catalyst sustained current densities of approximately 3.5 mA/cm² during the first hour of electrolysis (Figure S27), corresponding to TOF = 480 s^{–1} (see Supporting Information). This calculated TOF is significantly higher than the TOF calculated for $\text{Mn}(\text{bpy-}^t\text{Bu})(\text{CO})_3\text{Br}$ during CPE with 1.4 M TFE (270 s^{–1}).¹⁵ Current density fluctuated between 3.4 and 2.9 mA/cm² over the next ~6 h and gradually declined throughout the remainder of the experiment (total time of CPE was ~25 h). Faradaic efficiencies for CO production gradually dropped after the first few hours of electrolysis; however, no hydrogen production was observed throughout the entire experiment.

CPE under N₂ with 0.3 M TFE was performed in order to prove that the observed CO did not result from degradation of catalyst **2** (Figure S27). The results of this CPE show that only a minuscule amount of CO (Faradaic efficiency of ~2%) and no H₂ was observed over the course of ~24 h. Therefore, within error, all observed CO in our CPE experiment under CO₂ resulted from the reduction of CO₂ rather than degradation of the catalyst. After ~1.15 × 10^{–4} moles of electrons were consumed, 5.87 × 10^{–5} moles of CO were produced for CPE under CO₂ and only 1.87 × 10^{–6} moles of CO were produced for CPE under N₂. Additionally, this experiment proves that the catalyst is extremely stable under the conditions of this CPE experiment over the course of ~24 h.

CO₂ Binding. In addition to catalytic current enhancement, CVs of **2** under CO₂ with added Brønsted acid show loss of reversibility at the two-electron reduction (Figure 7) and a shift of the reduction wave to more positive potentials (Figure 10, Table 2). Both of these characteristics are indicative of CO₂ binding to the Mn catalyst.³⁴ Gagne et al. and Fujita et al. have

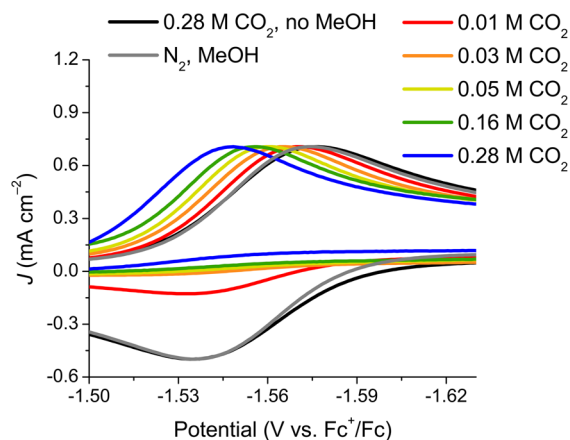


Figure 10. Cyclic voltammograms (CVs) of 1 mM $[\text{Mn}(\text{mesbpy})(\text{CO})_3(\text{MeCN})](\text{OTf})$ (**2**) showing evidence for CO_2 binding with 0.8 M MeOH. As the $[\text{CO}_2]$ increases from approximately 0 to 0.28 M, the cathodic peak potential of the two-electron reduction shifts to more positive potentials. In these CVs, the reverse oxidation scans are not shown in order to more clearly show the shift of the cathodic peak. CVs are taken at a scan rate of 100 mV/s.

Table 2. Cathodic Peak Potentials (E) in CVs^a of $[\text{Mn}(\text{mesbpy})(\text{CO})_3(\text{MeCN})](\text{OTf})$ (2**)^b under Various $[\text{CO}_2]$ and 0.8 M MeOH**

$[\text{CO}_2]^c$ (M)	E (V vs Fc^+/Fc)
0.00	-1.576
0.01	-1.571
0.03	-1.565
0.05	-1.561
0.16	-1.550
0.26	-1.546

^aCVs were taken in 0.1 M TBAPF₆/MeCN with a scan rate of 100 mV/s, a glassy carbon working electrode (3 mm diameter), a platinum wire counter electrode, and a Ag/AgCl wire pseudo-reference with ferrocene (Fc) added as an internal reference. ^b[**2**] = 1 mM. ^c $[\text{CO}_2]$ in MeOH taken from ref 22.

utilized eq 6 to calculate substrate binding constants (K_Q) for various copper, cobalt, and nickel macrocycles.^{34,35}

$$E = E^\circ + \left(\frac{RT}{nF}\right) \ln\{1 + [\text{CO}_2]K_Q\} \quad (6)$$

This equation describes an $E_{\text{R}}C_{\text{cat}}$ mechanism, where electron transfer and forward and backward reactions are sufficiently rapid and K_Q is relatively large. For complex **2**, we see no change in the two-electron reduction between CVs under N_2 or under CO_2 (without added H^+), indicating that CO_2 binding occurs only with the addition of an external proton source (Figure 10, Figure S29). CVs in Figure 10 and Figure S29 do not show the reversal potentials in order to more clearly show the shift of the cathodic peak. CVs show the same behavior whether the cathodic scan is reversed before or after the potential of the catalytic wave (see Figure 7). In CVs of **2**, we see irreversible behavior under CO_2/H^+ ; i.e., only the cathodic component of the voltammograms was observed. This feature is likely due to a $\text{Mn}(\text{I})-\text{CO}_2\text{H}$ species forming as a result of a two-electron oxidative addition of CO_2/H^+ to the Mn center of **4**. This $\text{Mn}(\text{I})-\text{CO}_2\text{H}$ species appears to be stable at these potentials once it is formed, which explains the irreversible behavior observed in CVs. Because of these characteristics, our

CVs are a limiting case of an $E_{\text{R}}C_{\text{cat}}$ scheme, where electron transfer and forward reactions are sufficiently rapid but the reverse reaction is slow. Although eq 6 applies to reversible kinetics, this analysis is sufficient to estimate a binding constant for CO_2/H^+ . The observed shift in potential (ΔE) of the cathodic peak is not a linear function of $\ln[\text{CO}_2]$, consistent with a binding constant ($K_{\text{CO}_2/\text{H}^+}$) of $\leq 100 \text{ M}^{-1}$ (Figure S28).^{34b} An average $K_{\text{CO}_2/\text{H}^+} = 46 \pm 10 \text{ M}^{-1}$ was calculated for **2** using eq 6.

Infrared Spectroelectrochemistry (IR-SEC) under CO_2/H^+ . We utilized IR-SEC with added CO_2 and MeOH in order to elucidate why catalysis occurs at a potential ~ 400 mV more negative than the potential at which the two-electron reduced, anionic CO_2 -binding state is formed. The results of this IR-SEC experiment on complex **1** with 0.14 M CO_2 (half-saturated) and ~ 80 mM MeOH are shown in Figure 11. At approximately

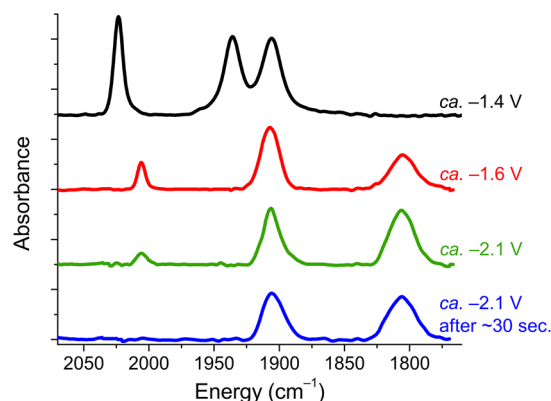


Figure 11. IR-SEC of 3 mM **1** in MeCN with 0.1 M TBAPF₆ electrolyte, ~ 0.14 M CO_2 (half-saturation), and ~ 80 mM MeOH. At approximately -1.4 V (black), **1** is the only species in solution ($\nu_{\text{CO}} = 2023, 1936, \text{ and } 1913 \text{ cm}^{-1}$). At the potential of the two-electron reduction (red), **1** fully converts into two new species, a $\text{Mn}(\text{I})-\text{CO}_2\text{H}$ tricarbonyl complex and anion **4**. The $\text{Mn}(\text{I})-\text{CO}_2\text{H}$ complex persists until the potential of catalysis (green), and this species fully disappears upon holding the cell at this potential (blue).

-1.4 V, complex **1** is the only species in solution with ν_{CO} stretches at 2023, 1936, and 1904 cm^{-1} . Upon reaching the potential of the two-electron reduction seen in CVs (approximately -1.6 V), we see complete conversion of complex **1** to two new species that, based on the ν_{CO} spectrum, must be a $\text{Mn}(\text{I})$ complex and anion **4**. Specifically, we see growth of ν_{CO} stretches at 2006, 1907, and 1806 cm^{-1} . Since the ν_{CO} band at 1907 cm^{-1} has a much greater intensity than either of the other bands, we believe two ν_{CO} stretches contribute to this line shape. The ν_{CO} stretches at 1907 and 1806 cm^{-1} match anion **4**. The other ν_{CO} stretches at 2006 and 1907 cm^{-1} are consistent with a $\text{Mn}(\text{I})$ tricarbonyl complex, likely a *fac*- $\text{Mn}(\text{I})$ tricarbonyl species. Upon reaching the potential of catalysis (approximately -2.1 V), the ν_{CO} stretches corresponding to this $\text{Mn}(\text{I})$ tricarbonyl species disappear, and the only species that persists is anion **4**. The ν_{CO} stretches of this $\text{Mn}(\text{I})$ tricarbonyl species (2006 and 1907 cm^{-1}) agree well with previously reported *fac*- Mn tricarbonyl complexes with bound ester groups and chelating diphosphine ligands,³⁶ as well as with previously reported *fac*- $\text{Re}(\text{bpy-R})(\text{CO})_3(\text{CO}_2\text{H})$ complexes.^{11,37} Bourrez et al. recently reported the characterization of a *mer*- $\text{Mn}(\text{II})(\text{dmbpy})(\text{CO})_3(\text{CO}_2\text{H})$ intermediate in the electrocatalytic CO_2 reduction studies of a $[\text{Mn}(\text{O})-$

(dmbpy)(CO)₃]₂ dimer.³⁸ A *mer*-Mn(I) tricarbonyl species would likely have at least one ν_{CO} stretch higher in energy than complex **1**.³⁹ Therefore, we are assigning the Mn(I) tricarbonyl species formed under two-electron reduction conditions in the presence of CO₂/H⁺ as *fac*-Mn(mesbpy)(CO)₃(CO₂H). Complexes of this type usually have a weak ν_{OCO} stretch between 1700 and 1500 cm⁻¹, but this stretch was not observed in our experiments likely because of the small accumulation of this Mn–CO₂H complex or because of overlapping ν_{OH} bends from added MeOH in this region. In addition to these IR-SEC experiments, reacting chemically reduced anion **4** with CO₂, followed by the addition of a small concentration of MeOH, results in a color change of the solution from dark blue to yellow-orange. This color change is consistent with the formation of a Mn(I) complex. Experiments are ongoing in our laboratory to independently synthesize, isolate, and fully characterize this Mn(I)–CO₂H species.

Since a Mn(I)–CO₂H species appears to be observed between the potentials of approximately –1.6 and –2.1 V, we have concluded that this species is responsible for the unusual “over-reduction” required to initiate catalysis. Again, by “over-reduction”, we mean that while **1** or **2** can be reduced by two electrons to form **4** and while **4** shows clear evidence for binding and reducing CO₂/H⁺, catalysis is not initiated until a third electron is introduced at approximately –2.0 V vs Fc⁺/Fc. Other possible intermediates that might have contributed to the high added potential could either be a formally Mn(I) or Mn(0) tetracarbonyl species. We see no evidence for the characteristic ν_{CO} pattern for tetracarbonyl species in our IR-SEC spectra, which further supports the identification of a Mn(I)–CO₂H species. We propose a simplified catalytic mechanism in Figure 12 that is consistent with all of our

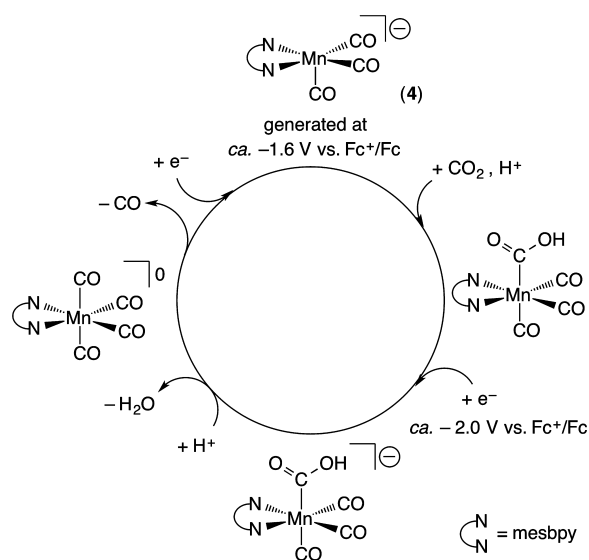


Figure 12. Proposed catalytic mechanism of [Mn(mesbpy)(CO)₃]⁻ (**4**) with CO₂ and H⁺, showing how reduction of a Mn(I)–CO₂H species can determine the overpotential for catalysis.

experimental observations. Here, after **1** is reduced to **4** at –1.6 V vs Fc⁺/Fc, anion **4** binds CO₂ with H⁺ forming the hydroxycarbonyl complex, Mn(I)(mesbpy)(CO)₃(CO₂H). This 18-e⁻ Mn(I)–CO₂H species is reduced at –2.0 V vs Fc⁺/Fc, likely through a bpy-based reduction, which is the source of the additional potential required for catalysis. After

being reduced, this species is a formally 19-e⁻ species, and thus, decomposition to CO and OH⁻, the latter of which rapidly reacts with H⁺, is believed to be extremely fast. This presumption is also supported by not observing any species other than anion **4** and the Mn–CO₂H species at the potential of catalysis in our IR-SEC experiments. Further reduction regenerates the catalytically active state **4**. This proposed mechanism is very similar to the mechanism of [Re(bpy-R)(CO)₃]⁻ complexes, reported recently by our group.^{11,13b} For these Re complexes, CO₂ and H⁺ bind rapidly to Re, and the resulting Re(I)–CO₂H complex must be reduced to continue the catalytic cycle.

CONCLUSIONS

We have described earth-abundant metal catalyst precursors Mn(mesbpy)(CO)₃Br (**1**) and [Mn(mesbpy)(CO)₃(MeCN)](OTf) (**2**), which show increased catalytic activity for the reduction of CO₂ to CO when compared to previously reported Mn(bpy-R)(CO)₃X complexes. In the electrochemistry of complexes **1** and **2**, we see no evidence for dimerization, indicating that the bulky mesbpy ligand possesses sufficient steric hindrance to eliminate dimerization at the Mn center. Eliminating dimerization results in atypical electrochemistry compared to standard Mn(bpy-R)(CO)₃X complexes. Typically, CVs of Mn bpy complexes show two one-electron reductions separated by ~300 mV. For complexes **1** and **2**, a single, reversible two-electron reduction wave is observed under N₂ at approximately –1.6 V vs Fc⁺/Fc. This two-electron reduction generates the anionic state, [Mn(mesbpy)(CO)₃]⁻ (**4**), at a potential of 300 mV more positive than in typical Mn bpy catalysts. We have characterized both complexes **1** and **4** by X-ray crystallography. IR-SEC of **1** under N₂ shows that both a singly reduced complex [Mn(mesbpy)(CO)₃]⁰ (**3**) and anionic complex **4** form at the same potential. Since a singly reduced species is observed in IR-SEC experiments, we believe that the two-electron reversible reduction seen in CVs of **1** and **2** is the result of two one-electron reductions rather than a direct two-electron reduction. This conclusion is consistent with chemical reductions with KC₈ and with DFT results.

Although anion **4** is generated at –1.6 V vs Fc⁺/Fc, catalysis does not occur until ~400 mV more negative, at approximately –2.0 V vs Fc⁺/Fc. CVs of **1** and **2** under CO₂ with added Brønsted acid show loss of reversibility at the two-electron reduction and a shift of this reduction wave to more positive potentials, indicative of CO₂ binding with H⁺ to complex **4**. IR-SEC experiments under CO₂ with added Brønsted acid indicate that reduction of a Mn(I)–CO₂H intermediate in the catalytic cycle may determine the unusual overpotential. A TOF of 5000 s⁻¹ ($i_{\text{cat}}/i_{\text{p}} = 50$) was calculated for catalyst **2** with 1.4 M TFE. A Faradaic efficiency of 98 ± 6% was observed for the formation of CO from CO₂ with 0.3 M TFE, with no observable production of H₂. At these activities, complexes **1** and **2** are more active than the best previously reported Mn bpy catalyst, Mn(bpy-*Bu*)(CO)₃Br. Although no decrease in catalytic overpotential was observed from previously reported Mn(bpy)-(CO)₃X, many synthetic strategies can be utilized to move the catalytic potential to a similar potential as substrate binding, including placing local proton sources or local hydrogen bonding interactions in the vicinity of the Mn center. The findings reported in this study provide new mechanistic and synthetic insights for improving catalysts in the future, with the ultimate goal of attaining a catalytic system capable of implementation on a large scale.

■ EXPERIMENTAL SECTION

General Considerations. NMR spectra were recorded on a Varian 300 MHz spectrometer at 298 K, and data were manipulated using Bruker TopSpin software. ^1H chemical shifts are reported relative to TMS ($\delta = 0$) and referenced against solvent residual peaks. Infrared spectra were collected on a Thermo Scientific Nicolet 6700 or a Bruker Equinox 55 spectrometer. Microanalyses were performed by Midwest Microlab, LLC (Indianapolis, IN) for C, H, and N. Solvents were sparged with argon, dried on a custom dry solvent system over alumina columns, and stored over molecular sieves before use. Manipulations of Mn complexes were covered from light. Potassium graphite (KC_8) was prepared according to literature methods and stored at $-30\text{ }^\circ\text{C}$ under dry nitrogen in a glovebox.⁴⁰ Tetrabutylammonium hexafluorophosphate (TBAPF_6 , Aldrich, 98%) was twice recrystallized from methanol (MeOH) and dried under a vacuum at $90\text{ }^\circ\text{C}$ overnight before use. 18-Crown-6 (Sigma Aldrich, 99%) was recrystallized from acetonitrile (MeCN) and dried under a vacuum at $90\text{ }^\circ\text{C}$ overnight before use. Other reagents were used as received: 6,6'-dibromo-2,2'-bipyridine (TCI America, >95%), 2,4,6-trimethylphenylboronic acid (Frontier Scientific), sodium bicarbonate (Na_2CO_3 , Macron Chemicals), tetrakis(triphenylphosphine)-palladium(0) ($\text{Pd}(\text{PPh}_3)_4$, Alfa Aesar, 99.8%), manganese pentacarbonyl bromide ($\text{Mn}(\text{CO})_5\text{Br}$, Alfa Aesar, 98%), and silver trifluoromethanesulfonate (AgOTf , Oakwood Products, 99%).

Synthesis of 6,6'-Dimesityl-2,2'-bipyridine (mesbpy). This ligand was synthesized in an analogous fashion to a previous report.¹⁷ To a toluene (250 mL) solution of 6,6'-dibromo-2,2'-bipyridine (4.00 g, 12.7 mmol), an excess of 2,4,6-trimethylphenylboronic acid (5.44 g, 33.1 mmol) suspended in 30 mL of MeOH was added. A 60 mL sample of 2 M Na_2CO_3 and $\text{Pd}(\text{PPh}_3)_4$ (2.3% mol cat.) were added to the reaction flask, and the mixture was refluxed for 72 h in air. After the mixture was cooled, the layers were separated. The organic layer was washed with brine ($3 \times 100\text{ mL}$), and the aqueous layer was washed with chloroform ($3 \times 100\text{ mL}$). The organic fractions were combined and dried under rotary evaporation. The resulting crude solid was dissolved in a minimal amount of hot chloroform and filtered. Methanol was added until a white precipitate crashed out from the filtrate. The white precipitate was filtered and dried overnight under vacuum at $80\text{ }^\circ\text{C}$. The yield of pure product was 3.56 g (71%). All characterization results matched those of previous reports¹⁷ and were consistent with the structure of the ligand.

Synthesis of $\text{Mn}(\text{mesbpy})(\text{CO})_3\text{Br}$ (1). $\text{Mn}(\text{CO})_5\text{Br}$ (200 mg, 0.73 mmol) was added to 50 mL of diethyl ether (Et_2O) in ambient air. The mesbpy (280 mg, 0.71 mmol) was added to the mixture and heated to reflux. The solution turned orange within 30 min, and the product precipitated out of solution. The mixture was cooled to room temperature, and the precipitate was filtered off and cleaned with Et_2O . The orange solid was dried overnight under vacuum. The yield of $\text{Mn}(\text{mesbpy})(\text{CO})_3\text{Br}$ was 308 mg (69%). X-ray quality crystals were grown from the vapor diffusion of pentane into a THF solution of the complex (Table 3). ^1H NMR (CD_3CN): $\delta = 2.08$ (s, 12H, CH_3), 2.34 (s, 6H, CH_3), 7.02 (s, 4H, phenyl H), 7.41 (d, 2H, 5,5' H, $J = 7\text{ Hz}$), 8.14 (t, 2H, 4,4' H, $J = 7\text{ Hz}$), 8.41 (d, 2H, 3,3' H, $J = 8\text{ Hz}$). IR (THF) ν_{CO} : 2021, 1940, 1906 cm^{-1} . Anal. Calcd for 1, $\text{C}_{31}\text{H}_{28}\text{BrMnN}_2\text{O}_3$: C, 60.90; H, 4.62; N, 4.58. Found: C, 60.58; H, 4.58; N, 4.53.

Synthesis of $[\text{Mn}(\text{mesbpy})(\text{CO})_3(\text{MeCN})](\text{OTf})$ (2). Complex 1 (500 mg, 0.82 mmol) was added to 80 mL of MeCN in a Schlenk flask in a nitrogen-filled, dry glovebox. AgOTf (233 mg, 0.90 mmol) was suspended in 20 mL of MeCN, and this solution was added in the flask. The reaction flask was brought out of the box, covered with foil (to avoid exposure to light), and heated to reflux overnight under a stream of N_2 . The reaction mixture was yellow/orange during reflux and had a black/brown solid at the bottom. After 18 h of reflux, the heat was removed, and the black/brown solid was removed by vacuum filtration. The filtrate was dried by rotary evaporation, yielding yellow/orange powder. The product was purified by flash chromatography with a Teledyne CombiFlash Rf by passing the mixture through a basic alumina column with MeCN as the eluent. The fractions were

Table 3. Crystallographic Data for $\text{Mn}(\text{mesbpy})(\text{CO})_3\text{Br}$ (1) and $[\text{Mn}(\text{mesbpy})(\text{CO})_3][\text{K}(18\text{-crown-6})]$ (4)

	$\text{Mn}(\text{mesbpy})(\text{CO})_3\text{Br}$ (1)	$[\text{Mn}(\text{mesbpy})(\text{CO})_3][\text{K}(18\text{-crown-6})]$ (4)
empirical formula	$\text{C}_{33}\text{H}_{32}\text{BrMnN}_2\text{O}_{3.5}$	$\text{C}_{47}\text{H}_{60}\text{KMnN}_2\text{O}_{10}$
formula weight	647.45	907.01
temperature (K)	100(2)	100(2)
wavelength (\AA)	0.710 73	1.541 78
space group	C_2/c (No. 15)	Cmca (No. 64)
<i>a</i> (\AA)	35.078(5)	21.4105(15)
<i>b</i> (\AA)	8.2392(11)	13.7151(8)
<i>c</i> (\AA)	22.640(3)	31.255(2)
α (deg)	90.00	90.00
β (deg)	115.873(9)	90.00
γ (deg)	90.00	90.00
volume (\AA^3)	5887.3(15)	9177.9(10)
<i>Z</i>	8	8
density, calcd (Mg/m^3)	1.461	1.313
μ (mm^{-1})	1.844	3.630
<i>R</i>	0.0363	0.0873
<i>R_w</i>	0.0855	0.1724

combined, and the solvent was removed by rotary evaporation, yielding a bright yellow-orange solid. The final yield of pure product was 405 mg (69%). ^1H NMR (CD_3CN): $\delta = 2.05$ (s, 12H, CH_3), 2.19 (s, 6H, CH_3), 2.35 (s, 3H, bound MeCN), 7.06 (s, 4H, phenyl H), 7.55 (d, 2H, 5,5' H, $J = 8\text{ Hz}$), 8.27 (t, 2H, 4,4' H, $J = 8\text{ Hz}$), 8.50 (d, 2H, 3,3' H, $J = 8\text{ Hz}$). IR (THF) ν_{CO} : 2038, 1956, 1926 cm^{-1} . Anal. Calcd for 2, $\text{C}_{34}\text{H}_{31}\text{F}_3\text{MnN}_3\text{O}_6\text{S}$: C, 56.59; H, 4.33; N, 5.82. Found: C, 56.52; H, 4.24; N, 5.93.

Chemical Reductions of $\text{Mn}(\text{mesbpy})(\text{CO})_3\text{Br}$. Solutions of $\text{Mn}(\text{mesbpy})(\text{CO})_3\text{Br}$ (1–10 mM) were prepared in THF in a nitrogen-filled, dry glovebox and cooled to $-35\text{ }^\circ\text{C}$. For one-electron reductions, KC_8 (1.3 equiv) was added to the solution, and the solution was allowed to warm to room temperature over 30 min. The solution was filtered over silica to remove any over-reduced, charged complex. Filtration afforded a dark red solution of the neutral $\text{Mn}(0)$ complex $[\text{Mn}(\text{mesbpy})(\text{CO})_3]^0$ (3). For two-electron reductions, 18-crown-6 (2.5 equiv) and KC_8 (2.3 equiv) were added to the solution, and the solution was allowed to warm to room temperature over 30 min. The solution was filtered, affording a dark blue solution of the anion, $[\text{Mn}(\text{mesbpy})(\text{CO})_3][\text{K}(18\text{-crown-6})]$ (4). NMR samples were prepared by repeating the described chemical reductions in $\text{THF}-d_8$.

Characterization of Complex 3. The instability of this complex did not allow for isolation as a solid. Additionally, 3 was not long-lasting in solution, and any attempts to isolate this species for characterization beyond IR spectroscopy (i.e., XRD) were unsuccessful. IR (THF) ν_{CO} : 1984, 1894, 1880 cm^{-1} .

Characterization of Complex 4. X-ray quality crystals were grown from the vapor diffusion of pentane into a THF solution of the complex (Table 3). ^1H NMR ($\text{THF}-d_8$): $\delta = 2.16$ (s, 12H, CH_3), 2.32 (s, 6H, CH_3), 3.57 (br s, 24H, $\text{K}[18\text{-crown-6}]$), 7.02 (s, 4H, phenyl H), 7.31 (d, 2H, 5,5' H, $J = 7\text{ Hz}$), 7.93 (t, 2H, 4,4' H, $J = 8\text{ Hz}$), 8.33 (d, 2H, 3,3' H, $J = 8\text{ Hz}$). IR (THF) ν_{CO} : 1917, 1815 cm^{-1} .

Electrochemistry. Electrochemical experiments were performed using a BASi Epsilon potentiostat. A single-compartment cell was used for all cyclic voltammetry experiments with a glassy carbon working electrode (3 mm in diameter from BASi), a Pt wire counter electrode, and a Ag/AgCl pseudo-reference. Ferrocene (Fc) was added as an internal reference. All electrochemical experiments were performed with 0.1 M TBAPF_6 as the supporting electrolyte. Electrochemical cells were shielded from light during experiments. All solutions were purged with N_2 or CO_2 before CVs were taken. "Bone dry" CO_2 run through a Drierite column was used for all electrochemistry experiments. Mn complex concentrations ranged from 0.5 to 5.0

mM, and experiments with CO₂ were performed at gas saturation (~0.28 M) in MeCN. For experiments with varying [CO₂], a solution of saturated CO₂ in MeCN was diluted to afford the appropriate [CO₂]. All potentials were referenced vs Fc/Fc⁺.

Bulk Electrolysis. Bulk electrolysis experiments (at approximately -2.2 V vs Fc⁺/Fc) were carried out in a 60 mL single-compartment cell with a custom Teflon top designed in our laboratory. The setup included a carbon rod working electrode (7.4 cm² surface area), a Pt wire counter electrode separated from the solution by a porous glass frit, and an Ag/AgCl pseudo-reference separated from the solution by a Vycor tip. A BASi Epsilon potentiostat was used to apply potential and record current. The bulk reductions were carried out in MeCN with various amounts of added Brønsted acid and 0.1 M TBAPF₆. Bulk electrolysis solutions were purged with CO₂ for 10 min prior to electrolysis. Solutions were constantly stirred and shielded from light throughout bulk electrolysis experiments. Gas analysis for bulk electrolysis experiments were performed using 1 mL sample injections on a Hewlett-Packard 7890A series gas chromatograph with two molsieve columns (30 m × 0.53 mm i.d. × 25 μm film). The 1 mL injection was split between two columns, one with N₂ as the carrier gas and one with He carrier gas, in order to quantify both CO and H₂ simultaneously in each run. Gas chromatography calibration curves were made by sampling known volumes of CO and H₂ gas.

Infrared Spectroelectrochemistry (IR-SEC). The design of the IR spectroelectrochemical cell used for these studies has been reported previously by our group.⁴¹ This cell was used for these experiments with one modification. Here, a cell with a 4.5 mm glassy carbon disk working electrode was used in place of the polished platinum working electrode. This modification ensures that IR-SEC conditions mimic those of CVs as closely as possible and ensures that CO₂ reduction on the Pt working electrode is eliminated. A more detailed design of this cell will be published in a future manuscript. All spectroelectrochemical experiments were carried out in a 0.1 M TBAPF₆ solution in MeCN, and all solutions were prepared under an atmosphere of dry nitrogen in a glovebox. Blank MeCN solutions with 0.1 M TBAPF₆ were used for the FTIR solvent subtractions. For experiments under CO₂, a solution of catalyst in TBAPF₆/MeCN was saturated with CO₂ (~0.28 M) and diluted in half by an N₂-sparged solution of TBAPF₆/MeCN, affording a solution of ~0.14 M CO₂. A Pine Instrument Company model AFCBP1 bipotentiostat or a Gamry Reference 600 series three-electrode potentiostat was used to affect and monitor thin layer bulk electrolysis.

X-ray Crystallography. The single crystal X-ray diffraction studies were carried out on a Bruker Kappa APEX-II CCD diffractometer equipped with Mo K α radiation ($\lambda = 0.71073 \text{ \AA}$) or a Bruker Kappa APEX CCD diffractometer equipped with Cu K α radiation ($\lambda = 1.54184 \text{ \AA}$). The crystals were mounted on a Cryoloop with Paratone oil, and data were collected under a nitrogen gas stream at 100(2) K using ω and φ scans. Data were integrated using the Bruker SAINT software program and scaled using the software program. Solution by direct methods (SHELXS) produced a complete phasing model consistent with the proposed structure. All non-hydrogen atoms were refined anisotropically by full-matrix least squares (SHELXL-97).⁴² All hydrogen atoms were placed using a riding model. Their positions were constrained relative to their parent atom using the appropriate HFIX command in SHELXL-97. Crystallographic data and structure refinement parameters are summarized in Table 3.

Density Function Theory (DFT) Calculations. DFT calculations were performed with the Amsterdam density functional (ADF) program suite (version 2012.01).⁴³ The triple- ζ Slater-type orbital TZ2P basis set was utilized without frozen cores for all atoms. Relativistic effects were included via the zeroth-order regular approximation (ZORA).⁴⁴ The BP86 functional and the local density approximation (LDA) of Vosko, Wilk, and Nusair (VWN)⁴⁵ were coupled with the generalized gradient approximation (GGA) corrections described by Becke⁴⁶ and Perdew⁴⁷ for electron exchange and correlation, respectively. Frequency calculations were performed to verify that the optimized geometries were at minima. Geometry optimized xyz coordinates and a sample input file are included in the Supporting Information.

■ ASSOCIATED CONTENT

■ Supporting Information

Crystallographic information in CIF format; additional information about CVs of **1** and **2**, catalysis with added H₂O and TFE, kinetics of the catalytic reactions, CPE, CO₂ binding, DFT calculations, and TOF calculations. This material is available free of charge via the Internet at <http://pubs.acs.org>.

■ AUTHOR INFORMATION

Corresponding Author

ckubiak@ucsd.edu

Present Address

[†]K.A.G.: Department of Chemistry, DePaul University, 1110 W. Belden Avenue, Chicago, Illinois, 60614, United States.

Notes

The authors declare no competing financial interest.

■ ACKNOWLEDGMENTS

This work was supported by the Air Force Office of Scientific Research through the MURI program under AFOSR Award FA9550-10-1-0572. A.D.N.'s summer undergraduate research at University of California, San Diego, was made possible by the 2013 STARS (Summer Training Academy through Research in the Sciences) program, funded by the University of California's Leadership Excellence through Advanced Degrees (UC LEADS) program. Dr. Charles Machan, Jesse Froehlich, and Mark Reineke are acknowledged for their helpful discussions.

■ REFERENCES

- (1) Benson, E. E.; Kubiak, C. P.; Sathrum, A. J.; Smieja, J. M. *Chem. Soc. Rev.* **2009**, *38*, 89–99.
- (2) Concepcion, J. J.; House, R. L.; Papanikolas, J. M.; Meyer, T. J. *Proc. Natl. Acad. Sci. U.S.A.* **2012**, *109*, 15560–15564.
- (3) Appel, A. M.; Bercaw, J. E.; Bocarsly, A. B.; Dobbek, H.; DuBois, D. L.; Dupuis, M.; Ferry, J. G.; Fujita, E.; Hille, R.; Kenis, P. J. A.; Kerfeld, C. A.; Morris, R. H.; Peden, C. H. F.; Portis, A. R.; Ragsdale, S. W.; Rauchfuss, T. B.; Reek, J. N. H.; Seefeldt, L. C.; Thauer, R. K.; Waldrop, G. L. *Chem. Rev.* **2013**, *113*, 6621–6658.
- (4) (a) Costentin, C.; Drouet, S.; Robert, M.; Savéant, J.-M. *Science* **2012**, *338*, 90–94. (b) Costentin, C.; Robert, M.; Saveant, J.-M. *Chem. Soc. Rev.* **2013**, *42*, 2423–2436. (c) Hawecker, J.; Lehn, J. M.; Ziessel, R. *J. Chem. Soc., Chem. Commun.* **1984**, 328–330. (d) Johnson, F. P. A.; George, M. W.; Hartl, F.; Turner, J. J. *Organometallics* **1996**, *15*, 3374–3387. (e) Morris, A. J.; Meyer, G. J.; Fujita, E. *Acc. Chem. Res.* **2009**, *42*, 1983–1994. (f) Smieja, J. M.; Benson, E. E.; Kumar, B.; Grice, K. A.; Seu, C. S.; Miller, A. J. M.; Mayer, J. M.; Kubiak, C. P. *Proc. Natl. Acad. Sci. U.S.A.* **2012**, *109*, 15646–15650. (g) Smieja, J. M.; Kubiak, C. P. *Inorg. Chem.* **2010**, *49*, 9283–9289. (h) Windle, C. D.; Perutz, R. N. *Coord. Chem. Rev.* **2012**, *256*, 2562–2570. (i) Wong, K.-Y.; Chung, W.-H.; Lau, C.-P. *J. Electroanal. Chem.* **1998**, *453*, 161–169. (j) Froehlich, J. D.; Kubiak, C. P. *Inorg. Chem.* **2012**, *51*, 3932–3934.
- (5) (a) Schulz, H. *Appl. Catal., A* **1999**, *186*, 3–12. (b) Krylova, A. Y. *Kinet. Catal.* **2012**, *53*, 742–746. (c) Glasser, D.; Hildebrandt, D.; Liu, X.; Lu, X.; Masuku, C. M. *Curr. Opin. Chem. Eng.* **2012**, *1*, 296–302.
- (6) (a) Lange, J.-P. *Catal. Today* **2001**, *64*, 3–8. (b) Frenzel, J.; Kiss, J.; Nair, N. N.; Meyer, B.; Marx, D. *Phys. Status Solidi B* **2013**, *250*, 1174–1190. (c) Martin, O.; Perez-Ramirez, J. *Catal. Sci. Technol.* **2013**, *3*, 3343–3352.
- (7) (a) Franke, R.; Selent, D.; Börner, A. *Chem. Rev.* **2012**, *112*, 5675–5732. (b) Ojima, I.; Tsai, C.-Y.; Tzamarioudaki, M.; Bonafoux, D. In *Organic Reactions*; John Wiley & Sons, Inc.: Hoboken, NJ, 2004; (c) Evans, D.; Osborn, J. A.; Wilkinson, G. *J. Chem. Soc. A* **1968**, 3133–3142.

- (8) Grice, K. A.; Kubiak, C. P. In *Advances in Inorganic Chemistry*; Aresta, M., van Eldik, R., Eds.; Academic Press: Waltham, MA, 2014; Vol. 66, pp 163–188.
- (9) (a) Hawecker, J.; Lehn, J.-M.; Ziessel, R. *J. Chem. Soc., Chem. Commun.* **1983**, 536–538. (b) Sullivan, B. P.; Bolinger, C. M.; Conrad, D.; Vining, W. J.; Meyer, T. J. *J. Chem. Soc., Chem. Commun.* **1985**, 1414–1416. (c) Hawecker, J.; Lehn, J. M.; Ziessel, R. *Helv. Chim. Acta* **1986**, 69, 1990–2012. (d) Cosnier, S.; Deronzier, A.; Moutet, J.-C. *J. Mol. Catal.* **1988**, 45, 381–391. (e) Kumar, B.; Smieja, J. M.; Kubiak, C. P. *J. Phys. Chem. C* **2010**, 114, 14220–14223. (f) Kumar, B.; Smieja, J. M.; Sasayama, A. F.; Kubiak, C. P. *Chem. Commun.* **2012**, 48, 272–274.
- (10) (a) Kurz, P.; Probst, B.; Spingler, B.; Alberto, R. *Eur. J. Inorg. Chem.* **2006**, 2006, 2966–2974. (b) Benson, E. E.; Kubiak, C. P. *Chem. Commun.* **2012**, 48, 7374–7376. (c) Grice, K. A.; Gu, N. X.; Sampson, M. D.; Kubiak, C. P. *J. Chem. Soc., Dalton Trans.* **2013**, 42, 8498–8503. (d) Benson, E. E.; Grice, K. A.; Smieja, J. M.; Kubiak, C. P. *Polyhedron* **2013**, 58, 229–234.
- (11) Sampson, M. D.; Froehlich, J. D.; Smieja, J. M.; Benson, E. E.; Sharp, I. D.; Kubiak, C. P. *Energy Environ. Sci.* **2013**, 6, 3748–3755.
- (12) Benson, E. E.; Sampson, M. D.; Grice, K. A.; Smieja, J. M.; Froehlich, J. D.; Friebel, D.; Keith, J. A.; Carter, E. A.; Nilsson, A.; Kubiak, C. P. *Angew. Chem., Int. Ed.* **2013**, 52, 4841–4844.
- (13) (a) Fujita, E.; Muckerman, J. T. *Inorg. Chem.* **2004**, 43, 7636–7647. (b) Keith, J. A.; Grice, K. A.; Kubiak, C. P.; Carter, E. A. *J. Am. Chem. Soc.* **2013**, 135, 15823–15829.
- (14) *CRC Handbook of Chemistry and Physics*, 92nd ed.; Haynes, W. M., Ed.; CRC Press: Boca Raton, FL, 2011–2012.
- (15) Smieja, J. M.; Sampson, M. D.; Grice, K. A.; Benson, E. E.; Froehlich, J. D.; Kubiak, C. P. *Inorg. Chem.* **2013**, 52, 2484–2491.
- (16) Bourrez, M.; Molton, F.; Chardon-Noblat, S.; Deronzier, A. *Angew. Chem., Int. Ed.* **2011**, 50, 9903–9906.
- (17) Schmittel, M.; Ganz, A.; Schenk, W. A.; Hagel, M. Z. *Naturforsch.* **1999**, 54b, 559–564.
- (18) Benson, E. E.; Rheingold, A. L.; Kubiak, C. P. *Inorg. Chem.* **2010**, 49, 1458–1464.
- (19) Benson, E. E. *Structural and Electronic Studies of Complexes Relevant to the Electrocatalytic Reduction of Carbon Dioxide*. Ph.D. Dissertation, University of California, San Diego, La Jolla, CA, 2012.
- (20) Staal, L. H.; Oskam, A.; Vrieze, K. *J. Organomet. Chem.* **1979**, 170, 235–245.
- (21) Tulyathan, B.; Geiger, W. E. *J. Am. Chem. Soc.* **1985**, 107, 5960–5967.
- (22) Wang, J. *Analytical Electrochemistry*, 3rd ed.; John Wiley & Sons, Inc.: Hoboken, NJ, 2006.
- (23) Hartl, F.; Rosa, P.; Ricard, L.; Le Floch, P.; Zálaiš, S. *Coord. Chem. Rev.* **2007**, 251, 557–576.
- (24) Addison, A. W.; Rao, T. N.; Reedijk, J.; van Rijn, J.; Verschoor, G. C. *J. Chem. Soc., Dalton Trans.* **1984**, 1349–1356.
- (25) (a) Gore-Randall, E.; Irwin, M.; Denning, M. S.; Goicoechea, J. M. *Inorg. Chem.* **2009**, 48, 8304–8316. (b) Scarborough, C. C.; Sproules, S.; Weyhermüller, T.; DeBeer, S.; Wieghardt, K. *Inorg. Chem.* **2011**, 50, 12446–12462.
- (26) Scarborough, C. C.; Wieghardt, K. *Inorg. Chem.* **2011**, 50, 9773–9793.
- (27) Gennaro, A.; Isse, A. A.; Vianello, E. *J. Electroanal. Chem.* **1990**, 289, 203–215.
- (28) Savéant, J.-M.; Vianello, E. *Electrochim. Acta* **1962**, 8, 905–923.
- (29) Espenson, J. H. *Chemical Kinetics and Reaction Mechanisms*; McGraw-Hill: New York, 1981.
- (30) Bard, A. J.; Faulkner, L. R. *Electrochemical Methods*; Wiley: New York, 1980.
- (31) Olmstead, W. N.; Margolin, Z.; Bordwell, F. G. *J. Org. Chem.* **1980**, 45, 3295–3299.
- (32) Bordwell, F. G. *Acc. Chem. Res.* **1988**, 21, 456–463.
- (33) Costentin, C.; Savéant, J.-M. *ChemElectroChem* **2014**, DOI: 10.1002/celc.201300263.
- (34) (a) Gagne, R. R.; Allison, J. L.; Ingle, D. M. *Inorg. Chem.* **1979**, 18, 2767–2774. (b) Fujita, E.; Creutz, C.; Sutin, N.; Szalda, D. J. *J. Am. Chem. Soc.* **1991**, 113, 343–353.
- (35) Gagne, R. R.; Ingle, D. M. *J. Am. Chem. Soc.* **1980**, 102, 1444–1446.
- (36) Mandal, S. K.; Ho, D. M.; Orchin, M. *Polyhedron* **1992**, 11, 2055–2063.
- (37) Gibson, D. H.; Yin, X. *J. Am. Chem. Soc.* **1998**, 120, 11200–11201.
- (38) Bourrez, M.; Orio, M.; Molton, F.; Vezin, H.; Duboc, C.; Deronzier, A.; Chardon-Noblat, S. *Angew. Chem., Int. Ed.* **2014**, 53, 240–243.
- (39) (a) Stor, G. J.; Stufkens, D. J.; Vernooijs, P.; Baerends, E. J.; Fraanje, J.; Goubitz, K. *Inorg. Chem.* **1995**, 34, 1588–1594. (b) Uson, R.; Riera, V.; Gimeno, J.; Laguna, M.; Gamasa, M. P. *J. Chem. Soc., Dalton Trans.* **1979**, 996–1002.
- (40) Schwindt, M. A.; Lejon, T.; Hegedus, L. S. *Organometallics* **1990**, 9, 2814–2819.
- (41) Zavarine, I. S.; Kubiak, C. P. *J. Electroanal. Chem.* **2001**, 495, 106–109.
- (42) Sheldrick, G. *Acta Crystallogr., Sect. A* **2008**, 64, 112–122.
- (43) (a) Fonseca Guerra, C.; Snijders, J. G.; te Velde, G.; Baerends, E. J. *Theor. Chem. Acc.* **1998**, 99, 391–403. (b) te Velde, G.; Bickelhaupt, F. M.; Baerends, E. J.; Fonseca Guerra, C.; van Gisbergen, S. J. A.; Snijders, J. G.; Ziegler, T. *J. Comput. Chem.* **2001**, 22, 931–967. (c) SCM, Theoretical Chemistry, Vrije Universiteit, Amsterdam, The Netherlands.
- (44) (a) van Lenthe, E.; Baerends, E. J.; Snijders, J. G. *J. Chem. Phys.* **1993**, 99, 4597–4610. (b) Lenthe, E. v.; Snijders, J. G.; Baerends, E. J. *J. Chem. Phys.* **1996**, 105, 6505–6516.
- (45) Vosko, S. H.; Wilk, L.; Nusair, M. *Can. J. Phys.* **1980**, 58, 1200–1211.
- (46) Becke, A. D. *Phys. Rev. B* **1988**, 38, 3098.
- (47) (a) Perdew, J. P. *Phys. Rev. B* **1986**, 33, 8822–8824. (b) Perdew, J. P. *Phys. Rev. B* **1986**, 34, 7406–7406.